Evaluation of a Wind-Wave System for Ensemble Tropical Cyclone Wave Forecasting. Part I: Winds

STEVEN M. LAZARUS, SAMUEL T. WILSON, MICHAEL E. SPLITT, AND GARY A. ZARILLO

Florida Institute of Technology, Melbourne, Florida

(Manuscript received 17 May 2012, in final form 13 September 2012)

ABSTRACT

A computationally efficient method of producing tropical cyclone (TC) wind analyses is developed and tested, using a hindcast methodology, for 12 Gulf of Mexico storms. The analyses are created by blending synthetic data, generated from a simple parametric model constructed using extended best-track data and climatology, with a first-guess field obtained from the NCEP–NCAR North American Regional Reanalysis (NARR). Tests are performed whereby parameters in the wind analysis and vortex model are varied in an attempt to best represent the TC wind fields. A comparison between nonlinear and climatological estimates of the TC size parameter indicates that the former yields a much improved correlation with the best-track radius of maximum wind r_m. The analysis, augmented by a pseudoerror term that controls the degree of blending between the NARR and parametric winds, is tuned using buoy observations to calculate wind speed root-mean-square deviation (RMSD), scatter index (SI), and bias. The bias is minimized when the parametric winds are confined to the inner-core region. Analysis wind statistics are stratified within a storm-relative reference frame and by radial distance from storm center, storm intensity, radius of maximum wind, and storm translation speed. The analysis decreases the bias and RMSD in all quadrants for both moderate and strong storms and is most improved for storms with an r_m of less than 20 n mi. The largest SI reductions occur for strong storms and storms with an r_m of less than 20 n mi. The NARR impacts the analysis bias: when the bias in the former is relatively large, it remains so in the latter.

1. Introduction

Various studies have demonstrated the importance of the surface wind field in wave forecasts (e.g., Janssen et al. 1997; Makin and Kudryavtsev 1999; Young 2003). Due to advancements in meteorological modeling, increased availability of measured wind data over the ocean surface, and improved methods for integrating observations with model-generated wind fields, the quality of wind input that is available for use in both wave forecasting and hindcasting has vastly improved over the past several decades. There has also been improvement in the wave models, evolving from second to third generation (e.g., Holt and Hall 1992). However, despite progress in wave modeling, problems persist. This is especially apparent in the specification of wave heights in very high sea states, as well as large errors in

the specification of 2D wave spectra in complicated wave regimes such as tropical cyclones (Cardone et al. 2000). In particular, the issues germane to the work presented here are 1) the failure to resolve subgrid-scale flow features in extreme events such as tropical cyclones (TCs) and 2) extreme wind events outside the range for which the wave models are tuned. Although the hindcast methodology has been used extensively to tune wave models for tropical cyclones, the forecast applications have been somewhat limited. Given the potential high impact and relatively large uncertainty of TC intensity forecasts, ensembles are now also beginning to take root in operational wave forecasting (e.g., Roulston et al. 2005; Chen 2006). Probabilistic wave forecasts may ultimately be more useful in extreme wind events, but in order for the ensemble approach to be viable, the forecasts should be free of bias (e.g., Hamill 2000).

Wave hindcasting can be computationally expensive, especially when high-resolution atmospheric models are used to generate the surface wind field (Cardone et al. 2000). Here, an efficient method by which to produce a TC wind analysis using hindcasts is developed and

Corresponding author address: Steven M. Lazarus, Florida Institute of Technology, 150 W. University Blvd., Melbourne, FL 32901.
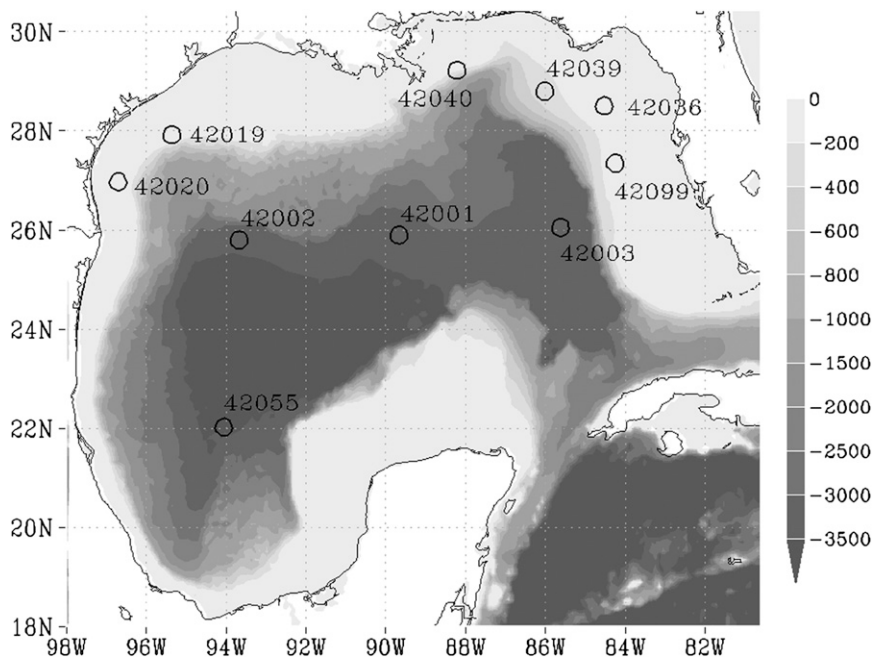E-mail: slazarus@fit.edu

FIG. 1. Location of the verification buoys (open circles) and bottom topography (m, shading).

evaluated. The approach taken is designed to minimize errors in the significant wave height by reducing the wind speed bias, with the eventual goal of generating operational ensemble wave forecasts. The cost-effective approach combines output from a simple parametric-derived wind field with background (i.e., first guess) winds from a large-scale NWP model (e.g., Desjardins et al. 2004; Mousavi et al. 2009). The parametric model is used to replace the poorly resolved first-guess inner-core wind field. Using hindcasts, the parametric model is constructed and tuned with observations from the "extended best track" dataset (DeMuth et al. 2006) and wind measurements from National Data Buoy Center (NDBC) buoys. A total of 12 Gulf of Mexico (GOM) TC events of varying intensities are examined. The data used to generate the wind analyses, the National Centers for Environmental Prediction–National Center for Atmospheric Research (NCEP–NCAR) North American Regional Reanalysis (NARR; Kalnay et al. 1996), and the best track are described in sections 2b and 2c, respectively. The parametric model, described in section 3a, is based on a modified asymmetric Rankine vortex described by Knaff et al. (2007, hereafter K07). The analysis wind fields are generated via blending the parametric model with the coarse-resolution NARR. The blending technique is described in detail in sections 3b and 3c. Systematic tests are performed whereby parameters in both the wind analysis and vortex model are varied in an attempt to best represent the TC wind fields

(sections 4a–c). In section 4d, analysis wind statistics are stratified within a storm-relative reference frame as well as by radial distance from storm center, storm intensity, translation speed, and radius of maximum wind.

2. Data

a. Buoy

To evaluate analysis wind speeds, the output is interpolated to the locations of 10 NDBC buoys (Fig. 1). Buoy latitude, longitude, depth (m), period of data availability, and anemometer height (m) are shown in Table 1. To limit any shallow-water influence on the waves (Lazarus et al. 2013, hereafter Part II), only those buoys in water depths greater than 50 m are used here. Wind speeds measured by NDBC buoys with anemometers that do not reach 10 m in height are adjusted using the power law with the exponent set equal to 0.11 (Hsu et al. 1994). This method has been shown to be acceptable in conditions of near-neutral stability. Measured wind speeds from 3-m discus buoys can experience low bias in extreme sea states (Cardone et al. 2007, International Ocean Vector Winds Science Team) as a result of wave sheltering, buoy motion, and other factors (Gilhousen 2006). Cardone et al. (1999) suggest that wind gust measurements from these buoys are a more reasonable measure of the true sustained wind speed in extreme conditions. Gilhousen (1987) evaluated

TABLE 1. GOM NDBC buoys used for evaluation. Buoys selected are those that measure significant wave height and are in water depths > 50 m. Latitude and longitude locations correspond to the current buoy locations.

Buoy	Lat (°)	Lon (°)	Depth (m)	Period	Anemometer height (m)
42020	26.966	96.695	88.1	1990–present	5
42002	25.790	93.666	3566.2	1973–present	10
42001	25.888	89.658	3246.0	1975–present	5
42019	27.913	95.353	83.2	1990–2010	5
42040	29.212	88.207	274.3	1995–present	10
42036	28.500	84.517	54.5	1994–present	5
42039	28.791	86.008	307.0	1995–present	5
42099	27.340	84.245	93.9	2007–present	None
42003	26.044	85.612	3282.7	1976–present	10
42055	22.017	94.046	3380.5	2005–present	10

the performance of several NDBC buoys in tropical cyclones. The bias and standard deviation were both quite low in their "high wind" dataset, which included wind speeds up to 33 m s^{-1} for the dual-anemometer comparison and up to 20 m s^{-1} for the platform comparison. Calibration and comparison of stepped-frequency microwave radiometer (SFMR) performance is confined to GPS dropwindsonde (e.g., Uhlhorn et al. 2007), which appears to be a pragmatic approach given the problems with space–time syncing either of these with in situ buoys. Here, with the exception of the height adjustment, no other changes were made to the wind speeds measured by the NDBC buoys.

b. North American Regional Reanalysis (NARR)

The NARR is a 40-yr record of global atmospheric analyses that includes the assimilation of ship, aircraft, satellite, buoy, and other relevant data (Kalnay et al. 1996). The NARR has a horizontal grid of 32 km, 45 vertical levels, and is available at 3-h intervals from 1979 to the present. In a high-resolution wave modeling study over the North Atlantic, Cardone et al. (1999) showed that wave hindcasts forced with NARR winds were improved over those using the operational wind fields at NWP centers. While the quality and resolution of operational wind fields continues to increase, the NARR is used here because the adoption of a hindcast approach allows for the integration of a relatively data-rich global product. For operational purposes, the background wind field could be obtained from any of the suite of NCEP forecast models—with the most obvious candidate being the Global Forecast System (GFS) since its wind fields are not limited regionally. Regardless, the NARR and global atmospheric models still suffer from poor spatial resolution on the scale of TCs.

c. Extended best track

The extended best-track dataset, developed to serve as a supplement to the National Hurricane Center (NHC)

climatological TC database known as HURDAT, provides information regarding storm structure and size. The data include the radius of maximum wind speed, eye diameter, pressure and radius of the outer closed isobar, and maximum radial extent of the 34-, 50-, and 64-kt wind to the NE, SE, SW, and NW of storm center. The data for the Atlantic basin are available at 6-h intervals and extend back to 1988. The data used by the parametric model include the storm latitude; longitude; 1-min maximum sustained surface wind speed; the maximum radial extent of the 34-, 50-, and 64-kt wind in four quadrants; and the radius of maximum wind speed. These data were linearly interpolated to 3 h in order to match the availability of the NARR winds and to generate the subsequent wind forcing.

3. Models and analysis

a. Parametric wind field

A parametric model that employs climatology to predict TC wind radii estimates is used in this study. The simple model, based on a modified asymmetric Rankine vortex model of K07, is chosen as it approximates known structural TC variations and it provides a single methodology by which a baseline estimate of the TC wind field can be made given standard NHC best-track input. The parametric model is given by

$$V(r,\theta) = (v_m - a)\left(\frac{r_m}{r}\right)^x + a\cos(\theta - \theta_o) \quad \text{for} \quad r \geq r_m \quad \text{and}$$

$$V(r,\theta) = (v_m - a)\left(\frac{r}{r_m}\right) + a\cos(\theta - \theta_o) \quad \text{for} \quad r < r_m,$$

$$(1)$$

where $V(r, \theta)$ is the wind speed as a function of radial distance from storm center (r) and azimuth (θ), v_m is the maximum wind speed, r_m is the radius of maximum wind speed, x is a size parameter, a is the wavenumber 1

asymmetry magnitude, and θ_o is the degree of rotation of v_m from the direction 90° to the right of the storm motion vector. A storm motion–relative coordinate system, where azimuth is measured counterclockwise starting from the direction 90° to the right of the storm motion vector, is used here (K07). Equation (1) has one known parameter (v_m) and four free parameters (r_m, x, a, and θ_o). Using standard regression, K07 represent the free parameters as functions of climatological factors that are available in the best-track data (latitude, storm translational speed, and maximum wind speed).

b. Wind analysis theory

Wind analyses are generated via a combination of the NARR 10-m wind field (U_{10}) and the parametric model described by Eq. (1). The blending, based on a modified version of the successive corrections method (SCM; Cressman 1959; Barnes 1964), applies the NARR as the first guess and uses the parametric wind model to create synthetic observations on a 2-km grid. The basic idea is to replace the NARR's poorly resolved inner-core wind field with parametric winds while assuming that the NARR captures the wind speeds at distances farther away from the storm center. Pseudo observations are first generated using Eq. (1) and then spread, anisotropically, using the curvature of a parametric vortex model in lieu of the streamline curvature originally defined by Benjamin and Seaman (1985, hereafter BS85). The axisymmetric vortex model (DeMaria et al. 1992) is

$$V' = r' \exp\left[\frac{1}{b}(1 - r'^{b})\right], \qquad (2)$$

where V' and r' are the normalized tangential velocity (i.e., v/v_m) and radial distance from storm center (r/r_m), respectively, and b is a size parameter. Integrating Eq. (2) with respect to r' (to simplify the integration and its application, b is set equal to 1) yields

$$s \equiv \int_0^r V' \, dr' = \int_0^r r' \exp[(1 - r')] \, dr' = e^1 e^{-r}(1 + r). \quad (3)$$

The anisotropy factor is determined by subtracting (from 1) the absolute value of the difference in s between the grid point (i, j) and observation (k):

$$w_{ijk} = \exp\left(-\frac{d_m^2}{R^2}\right)(1 - |s_{ij} - s_k|), \qquad (4)$$

where R is the radius of influence and d_m is defined by Eq. (5) in BS85. Figure 2 illustrates the new weight
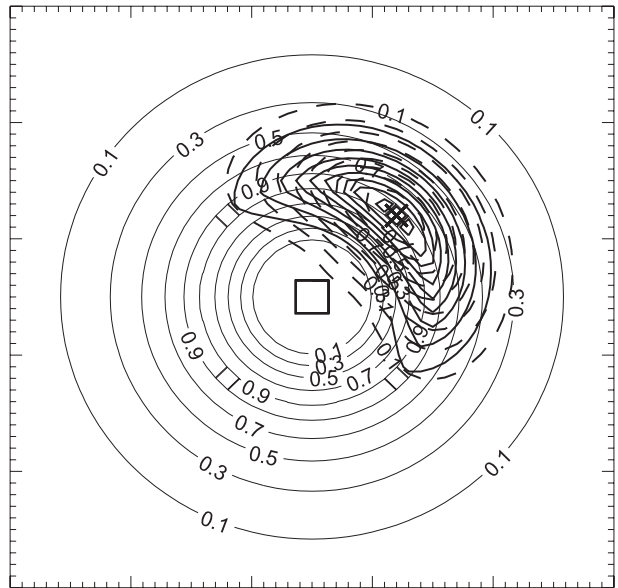

FIG. 2. Normalized parametric wind field (v/v_m, thin solid lines) based on Eq. (2), the Benjamin and Seaman banana weight (dashed lines), and a modified banana weight (thick solid lines) based on Eq. (4). Each of the weights is centered on an observation located at the ×.

[Eq. (4)] and the original banana weight of BS85 for an idealized TC wind field. The curvature in the modified weighting scheme is clearly enhanced over that of the banana-shaped weights of BS85, preferentially spreading the synthetic observation in the azimuthal direction.

A pseudoerror term is introduced into the analysis. To allow for operational flexibility, the error is based on the nth-order Butterworth low-pass filter (Butterworth 1930), which is defined as

$$H(\omega) \, H(\omega)^* = \frac{1}{1 + \left(\dfrac{\omega}{\omega_c}\right)^{2N}}, \qquad (5)$$

where $H(\omega) \, H(\omega)^*$ is the amplitude of the response function $R(\omega)$, ω is the distance from storm center, N is the filter order, and ω_c the cutoff distance. We define N and ω_c as

$$N = \frac{\ln\left(\dfrac{e}{\sqrt{A^2 - 1}}\right)}{\ln\left(\dfrac{\omega_p}{\omega_s}\right)} \qquad (6)$$

and

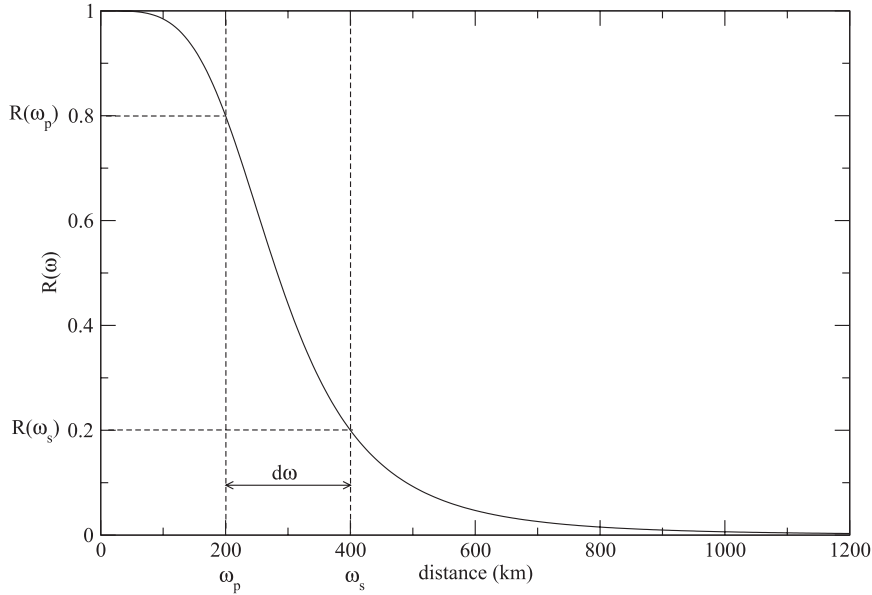$$\omega_c = \frac{\omega_p}{e^{1/N}}, \qquad (7)$$

FIG. 3. Butterworth filter example for which the response $R(\omega)$ at the start edge (ω_p) is 0.8, at the stop edge (ω_s) is 0.2, and $d\omega$ = 200 km. When $R(\omega)$ = 1 (0), the analysis is parametric (NARR) only.

where ω_p and ω_s are the pass and stop band edges, respectively; $A = 1/\sqrt{R(\omega_s)}$; and $e = 1/\sqrt{R(\omega_p) - 1}$. The user specifies ω_p, ω_s, $R(\omega_p)$, and $R(\omega_s)$, from which the filter order, cutoff distance, and response function can then be determined via Eqs. (5)–(7). An example

response curve is shown in Fig. 3. Because the objective is to inflate the observation error as the distance from the storm center increases so that the analysis is weighted more toward the background field (NARR), the observation (parametric) to background (NARR)
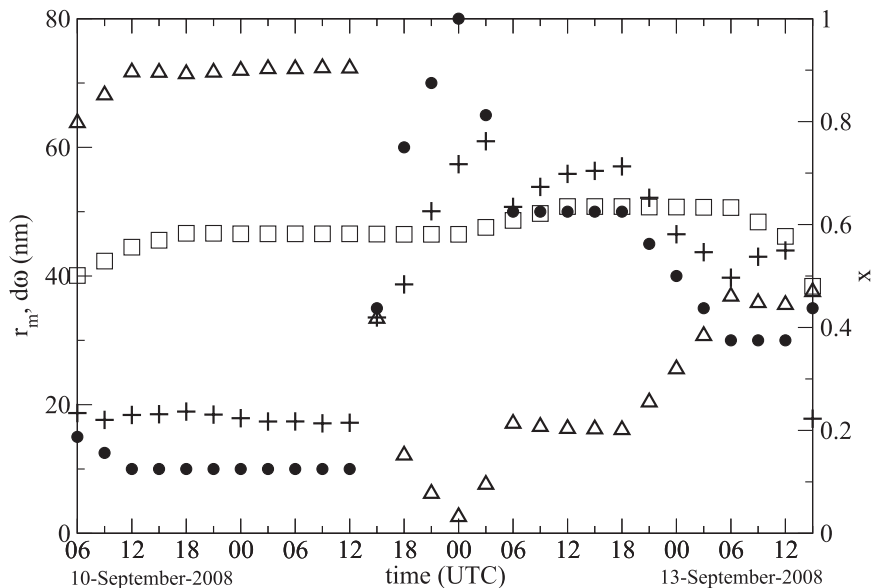

FIG. 4. The climatological size parameter x_c (open squares) and nonlinear size parameter x_n (plus signs) for TC Ike. Also shown is the best-track radius of maximum wind (n mi, black circles) and analysis filter width $d\omega$ (n mi, open triangles). See text for other parameter values.

error variance is set equal to the inverse square of Eq. (5).

c. Wind analysis application

The basic idea is to link the analysis parameters with observable (or forecast) quantities, ensuring functionality for operational applications. The pass edge ω_p of the response function is determined by setting $a = 0$ in Eq. (1) and solving for r such that

$$\omega_p = r_m \times \left(\frac{v_m}{v_t}\right)^{1/x}, \qquad (8)$$

where $r = \omega_p$ and $v = v_t$, which is a user-defined velocity for which the response function is reduced by $1 - R$ (ω_p). For the wind analyses presented in the following sections, v_t is set equal to v_m; thus, $\omega_p = r_m$ [Eq. (8)]. The response function value at $\omega_p[R(\omega_p)]$ is set equal to 0.99, resulting in an analysis that is heavily weighted to the parametric model at r_m. Both r_m and v_m are given in the best-track dataset while x is calculated indirectly using two different methodologies: 1) wind radii information and 2) climatology (K07; see following paragraph). The difference between the pass and stop ends of the filter ($\omega_s - \omega_p$), referred to as the filter width $d\omega$, is linearly related to the size parameter x; that is, $d\omega = D \times (d - x)$, where d is a constant (set equal to 2 here) and D is a nonlinear function of r_m defined as

$$D(r_m) = ar_m^2 - br_m + c, \qquad (9)$$

where a, b, and c are user-defined constants. In addition, D is designed to replace the TC inner core, which, in general, is poorly resolved by the coarse-resolution NARR—especially for tight storms (i.e., small r_m). Thus, for a fixed size parameter x, D and $d\omega$ decrease as r_m increases. Conversely, for fixed D (i.e., r_m fixed), as x increases (i.e., a decrease in the radial extent of the wind field), $d\omega$ decreases. In either case, the analysis transitions to the first-guess field (i.e., NARR) at smaller radii. Once $d\omega$ and ω_p are known, ω_s is calculated as a residual. The response function value at $\omega_s[R(\omega_s)]$ is set equal to 0.01, and thus the analysis at radii beyond the filter stop edge is essentially the background.

As previously mentioned, two different approaches are used to estimate the size parameter. In the first (where $x = x_c$), a multilinear regression equation that depends on maximum wind speed and latitude is used [K07, Eq. (2)]. The coefficients used are the climatological values given for the North Atlantic in K07 (see their Table 1). The climatology is based on a least squares method that minimizes the squared difference
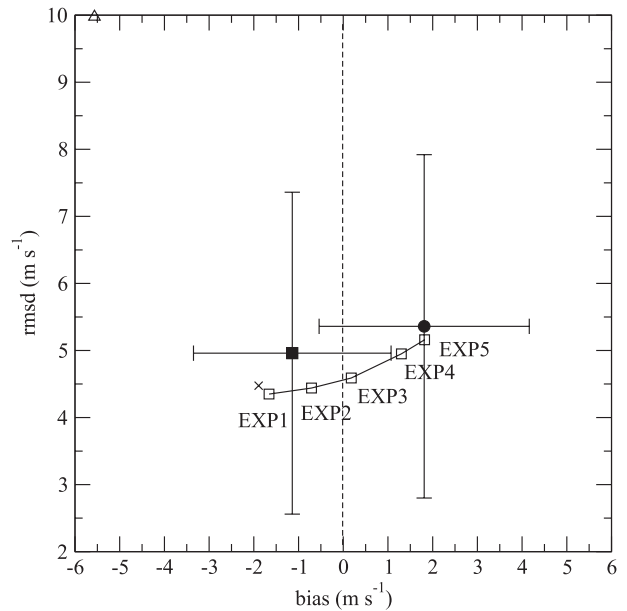

FIG. 5. Composite statistics for wind speed bias (m s^{-1}) vs RMSD (m s^{-1}) within 100 n mi of storm center for TCs Ike, Ivan, Rita, and Katrina. Here, $v_t = v_m$, $x = x_n$, and D [Eq. (9)] is set to linear ($a = 0.0$, $b = 0.5$) for the five experiments shown. Values for c [Eq. (9)] are 50, 75, 100, 150, and 200 n mi for experiments 1–5, respectively. Also shown are the statistics for all 12 storms for c equal to 100 n mi (filled circle) and quadratic D with c equal to 50 (and $a = 0.005$, $b = 1$; filled square). The $\times$ and open triangle symbols depict the four-storm subset for the quadratic D and the NARR, respectively. Zero bias is depicted by the dashed line.

between observed and analytic wind radii over a 16-yr period (1988–2003). It is also possible to take direct advantage of the radial quadrant information (i.e., the maximum radial extent of the 34-, 50-, and 64-kt wind in four quadrants) in the best-track data. A nonlinear size parameter ($x = x_n$) is calculated by simultaneously fitting the three wind radii in each of the four quadrants and solving Eq. (1) using the least squares method of differential evolution (Storn and Price 1997; Mishra 2007). In this case, both the asymmetry factor (a) and the degree of rotation (θ_o) are determined using their climatological values [i.e., Eq. (2) and Table 1 in K07] and r_m is obtained from the best-track data. Given the number of points (there is a maximum of 12) from which the size estimate is made, this limits the degrees of freedom to one and produces a stable solution. In addition, of the three remaining free parameters [in Eq. (1)], tests (not shown) indicate that x appears to exhibit a more direct correlation with the best-track TC wind radii, which are based on a poststorm analysis of all available information. In particular, as will be shown, x_n yields an improved wind analysis compared to that produced by x_c. Experiments where both a and x were fit
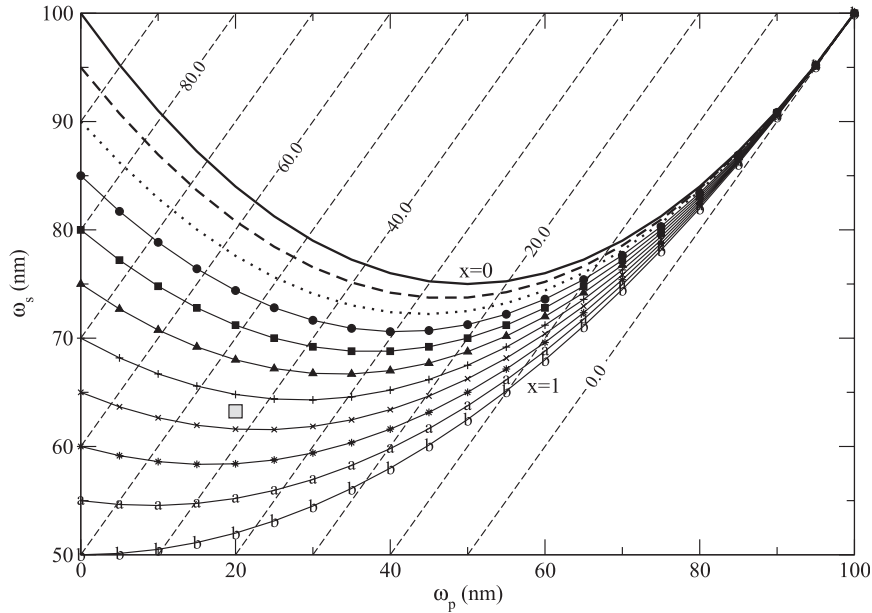
FIG. 6. The filter parameter space (ω_p vs ω_s, n mi) using the quadratic D [Eq. (9)] and size parameters ranging from 0.0 to 1.0 (in increments of 0.1), $R(\omega_p) = 0.99$, $R(\omega_s) = 0.01$, and $c = 50$ n mi. Here, $v_t = v_m$ and $\omega_p = r_m$ [Eq. (8)]. For example, the filter width $d\omega$ (dashed lines) is 100 n mi if both x and $r_m = 0$. The gray box is the filter width for the analysis shown in Fig. 7b.

simultaneously, and for a only (i.e., with $x = x_c$), were also attempted; however, the results were noisy. Ultimately, the size parameter is considered a priority here because the best-track TC wind radii are directly related to the observed storm size. Estimates of the nonlinear size parameter could also be generated using the forecast permutations in track, intensity, and structure from the NHC's Monte Carlo model (DeMaria et al. 2009), making this a viable approach with respect to generating ensemble wind analyses. This is discussed further in section 5.

4. Results

a. Size parameter

Estimates of the size parameters x_n and x_c are compared with the best-track r_m over an 81-h window for Hurricane Ike (Fig. 4). It is not surprising that x_n (plus signs) is sensitive to variations in r_m (black circles) while x_c is not (open squares). For example, during the 12-h period beginning 1200 UTC 11 September when Ike is undergoing an eyewall replacement, r_m increases from 10 to 80 n mi with a corresponding increase in x_n (from 0.2 to 0.8) while x_c remains constant (approximately 0.6). The r^2 value for x_n (versus r_m) is considerably larger than those for x_c (0.79 and 0.13, respectively). One might

actually expect a smaller size parameter as r_m increases. However, during the eyewall replacement cycle, the 34-, 50-, and 64-kt wind radii [V and r; Eq. (1)], the maximum wind speed (v_m), and the asymmetry coefficient [a; Eq. (1)] are relatively constant and thus an increase in r_m results in a larger x_n.

b. Filter width and shape

Using data from four TCs (Katrina, Rita, Ivan, and Ike), the impact of changes in D [Eq. (9)] on the wind analysis is evaluated. Bias, scatter index (SI, defined here as the ratio of the standard deviation of the differences to the mean of the measurements) and root-mean-square deviation (RMSD) are calculated using 10 GOM buoys (Fig. 1, Table 1) and are confined to observations within 100 n mi of the storm center. Five experiments are performed where D is linearly related to r_m ($a = 0.0$, $b = 0.5$, and $c = 50, 75, 100, 150,$ and 200 n mi) and one for which D and r_m are related via a quadratic fit ($a = 0.005$, $b = 1$, $c = 50$ n mi). Results are shown in Fig. 5, where EXP1–EXP5 (open squares) correspond to the wind analyses created using the linear D, $\times$ denotes the analyses generated using the quadratic relationship, and the NARR-only results are depicted by the open triangle. Also shown are the results for all 12 storms using the linear fit from EXP3, which produced the lowest bias of the four-storm subset (filled circle) and
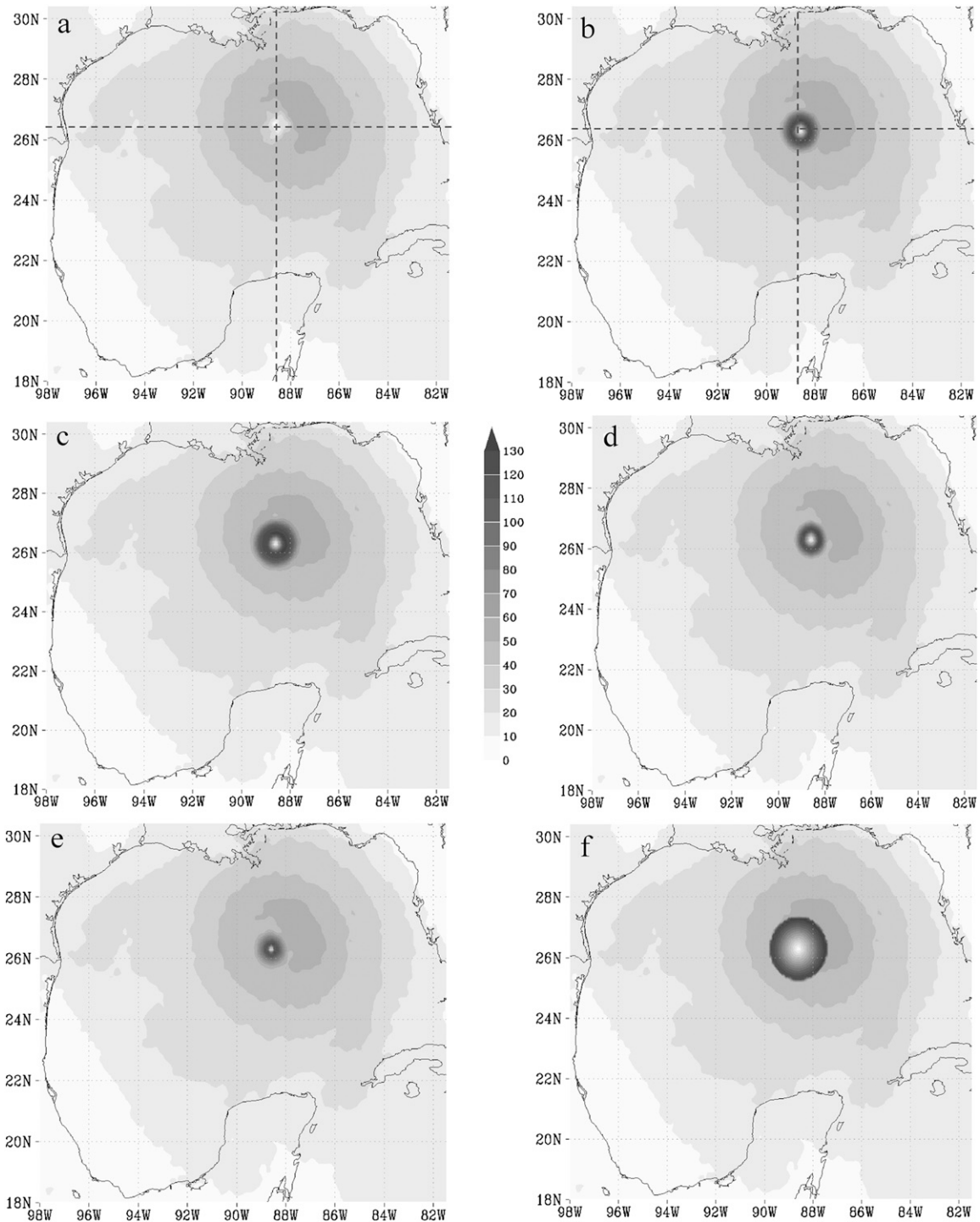
FIG. 7. Values of U_{10} (kt) for Hurricane Katrina valid 1800 UTC 28 Aug 2005: (a) NARR only, (b) AOC using best-track parameters and x_n, (c) analysis with $x = 0.2$ (EXPA; Table 2), (d) $x = 1.0$ (EXPB; Table 2), (e) analysis with $r_m = 10$ n mi (EXPC; Table 2), and (f) analysis with $r_m = 60$ n mi (EXPD; Table 2).

the quadratic fit (filled square). All of the wind analyses are a significant improvement over that of the NARR-only analysis. For the four-storm subset, the bias is lowest for EXP3 ($c = 100$ n mi), while the RMSD is lowest for EXP1 ($c = 50$ n mi; Fig. 5). The bias, clearly more sensitive to variations in c, changes sign with a range of 4 m s^{-1}, compared to less than 1 m s^{-1} for the RMSD. The parameter selection that produces the

lowest bias for the four storms (EXP3) yields a higher bias for all storms (filled circle), but it does fall within the bias envelope of the five experiments. A single standard deviation (cross hairs in Fig. 5) is shown for the 12-storm composites. Given the relatively large spread, it might also be prudent to allow for variations in c as well. Regardless, there appears to be a sweet spot, a blending width that minimizes the analysis bias. The quadratic fit is selected here as the analysis of choice (AOC) as it yields a lower wind speed bias and RMSD compared to the wind analyses from EXP3 when extended to all storms. This does not mean that the AOC is optimal for any one particular analysis; rather it is only true in the bulk sense. Also, the AOC will invariably depend on the quality, number, and distribution of the verifying observations—a limitation here.

The resulting filter parameter space (ω_p, ω_s) using the quadratic D is shown in Fig. 6 for size parameters ranging from 0.0 to 1.0, $R(\omega_p) = 0.99$, and $R(\omega_s) = 0.01$. The maximum $d\omega$ is 100 n mi if both x and $r_m = 0$. The size of $d\omega$ is relatively large for small x (i.e., large storm) and/or small r_m, but is more sensitive to variations in the latter. As r_m increases, all size parameters converge toward a zero filter width (i.e., a NARR-only wind analysis), and do so more rapidly for small x. For example, consider Hurricane Ike during 0600–1800 UTC 12 September 2008, where r_m is constant (50 n mi) but x_n increases from 0.63 to 0.71. In this case, $d\omega$ decreases only slightly from 17 to 16 n mi (open triangles in Fig. 4). Conversely, a 5-n mi decrease in r_m during 0600–1200 UTC 10 September 2008 while x_n is approximately constant (0.22) produces a larger change in $d\omega$, increasing from 64 to 72 n mi. The abrupt change in the parameters captures the eyewall replacement cycle in which the inner wind maximum dissipates and the outer wind maximum contracts, becoming the more dominant feature by 1800 UTC 11 September 2008 (Berg 2009).

c. Sensitivity experiments

Four sensitivity tests, using Hurricane Katrina, are performed to ensure that the modeled TC wind field responds appropriately to variations in x and r_m. As previously discussed, variations in r_m have a more pronounced effect on $d\omega$, which should be apparent in the gridded wind fields. Experiments are performed in which x is varied within the bounds of climatology (0.2 and 1.0) while holding r_m constant (15 n mi). Two additional tests are conducted in which r_m is set to 10 and 60 n mi while fixing x (0.5). For comparison purposes, the NARR-only results and the AOC generated using the best-track data are also shown. The resulting wind analyses (valid 1800 UTC 28 August 2008) and related

TABLE 2. Parameters and values for sensitivity tests in which x and r_m are systematically varied. For all experiments, $R(\omega_p) = 0.99$ and $R(\omega_s) = 0.01$. See text for details.

Parameter	Expt			
	A	B	C	D
x	0.2	1.0	0.5	0.5
r_m (n mi)	15	15	10	60
ω_p (n mi)	15	15	10	60
D (n mi)	36.1	36.1	40.5	8.0
$d\omega$ (n mi)	65.0	36.1	60.8	12.0
ω_s (n mi)	80.0	51.1	70.8	62.0

parameters are shown in Fig. 7 and Table 2, respectively. The NARR wind field is poorly resolved in this case with peak winds (60 kt) well below the observed (150 kt). The impact of the size parameter on the analysis is as expected, with a shrinking inner-core wind field as x increases. The peak wind speeds for the analysis are much higher, are closer to the observed, and wrap around the northern semicircle to the northwest of the center for $x = 0.2$. An increase in r_m results in an outward expansion of the highest winds in the storm core. The AOC, which is produced by using the r_m and nonlinear size parameter derived from the wind radii in the best-track data ($r_m = 20$, $x_n = 0.65$), yields a relatively tight core. Because the filter parameters are fixed for these experiments, all of the analyses quickly relax to the NARR outside of the 100-n mi radius.

An additional wind analysis (not shown in Fig. 7) is generated for Katrina using x_c (=0.94) for comparison. Figure 8 depicts north–south and west–east transects through the storm center (dashed lines in Figs. 7a and 7b) and includes the NARR, H*Wind (see next section), EXP3, EXP5, and x_n analyses. Compared to x_c, the x_n analysis produces a marginally broader storm with slightly higher winds that are closer to the best-track peak wind speed. With the exception of the eastern transect, the difference between the NARR winds (dashed line) and the best-track TC wind radii (open circles) increases inward. The inner-core structure of the AOC (i.e., within 50 n mi) and H*Wind are quite similar; however, both EXP3 and EXP5 exhibit a better overall fit than the AOC and do not have the "undershoot" seen on the north side of the AOC. These two experiments have a smoother transition from the parametric model to the NARR. If we examine the statistics for Katrina only (not shown), we find that the best analysis comes not from the AOC, but rather from EXP3. The AOC is defined from a bulk set of statistics that minimize the bias in the entire storm set and, thus, will be suboptimal for some of the analyses. Even though the analysis has built-in degrees of freedom (i.e.,
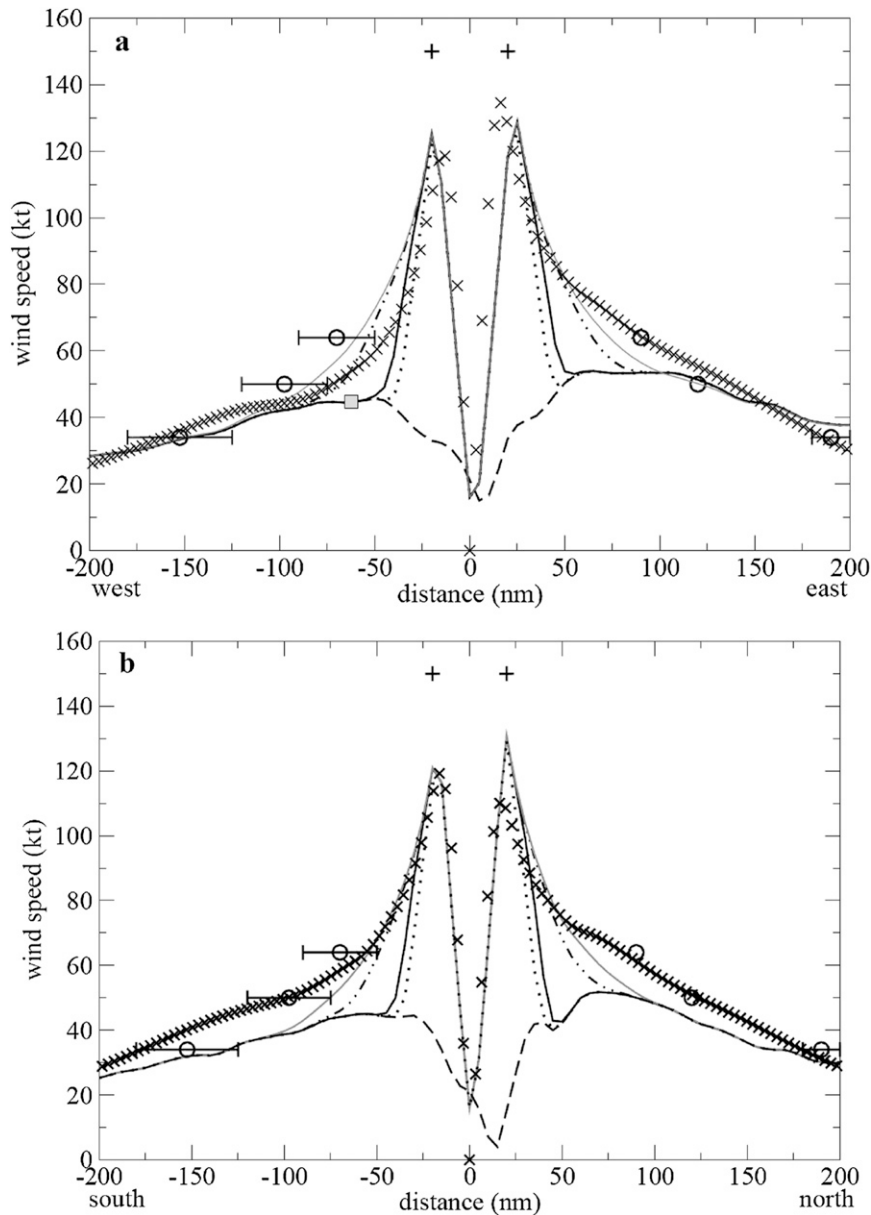
FIG. 8. The U_{10} (kt) (a) west–east and (b) south–north cross sections taken along the lines shown in Fig. 7a (NARR only, dashed line) and Fig. 7b (analysis with nonlinear size parameter, solid line). Also shown are the wind analysis using the climatological size parameter (dotted line), EXP3 (dashed–dotted line), EXP5 (solid gray line), HWIND ($\times$), the average 34-, 50-, and 64-kt best-track wind radii and their spread (open circles, horizontal error bars), buoy 42001 wind speed valid 1800 UTC 28 Aug 2005 [gray square box in (a)], and the best-track maximum wind ($+$). See text for details.

x and r_m) in an effort to capture storm-to-storm variability, the AOC snapshot shown is not the ''best'' analysis for this time (hence the term AOC rather than ''optimal'' or best, etc.). It is worth pointing out that EXP5, which appears to be a better fit to the best track and H*Wind, is not the best analysis for Katrina overall. The 1800 UTC 28 August 2005 buoy (42001) observation

(square box in Fig. 8a), which is located 63 n mi west of the storm, is consistent with the NARR and supports the tighter analysis (compared to H*Wind and the best-track wind radii), at least on the west side of the storm. The filter width, for the AOC in Fig. 7b, is on the order of 43 n mi (gray box in Fig. 6). Hence, the stop edge of the filter is near 60 n mi (i.e., $\omega_s = d\omega + r_m$, where $r_m = 20$ n mi),

TABLE 3. Strong TCs (Saffir–Simpson categories 3–5).

Storm	Saffir–Simpson category	Evaluation period
Opal (1995)	4	1800 UTC 27 Sep–1800 UTC 5 Oct
Isidore (2002)	3	1800 UTC 17 Sep–0600 UTC 27 Sep
Lili (2002)	4	1200 UTC 30 Sep–1200 UTC 4 Oct
Ivan (2004)	5	1200 UTC 10 Sep–0900 UTC 17 Sep
Dennis (2005)	4	1200 UTC 7 Jul–1200 UTC 12 Jul
Katrina (2005)	5	0000 UTC 24 Aug–1200 UTC 30 Aug
Rita (2005)	5	1200 UTC 19 Sep–1200 UTC 25 Sep
Gustav (2008)	4	0000 UTC 30 Aug–0000 UTC 4 Sep

which is evident with the analysis relaxing to the NARR at a radius of approximately 60 n mi. Any discrepancies in the NARR winds outside ω_s will remain in the wind analysis.

d. Wind analysis evaluation

For a few representative cases, the AOC storm structure is compared to tropical cyclone wind analyses generated by the Hurricane Research Division. The product, referred to as H*Wind, blends available data including aircraft reconnaissance, dropsonde, buoy, and Coastal-Marine Automated Network (C-MAN) platforms (Powell et al. 1998). The wind data are processed within a storm-relative framework and reduced to a common 10-m reference height. Rather than a snapshot, an H*Wind analysis represents the TC wind field over a window ranging from 4 to 6 h. Bias (analysis–background minus observed wind speed), RMSD, and SI statistics are also presented in which the AOC is compared against wind measurements from 10 NDBC buoys (Table 1). NARR wind error statistics are also provided for comparison purposes. The 12 TCs evaluated in this study are split into two categories based on maximum storm strength (i.e., Saffir–Simpson category) in the GOM. TCs of categories 3–5 are referred to as strong (Table 3), and categories 1–2 as moderate (Table 4).

1) H*WIND COMPARISON

The 10-m wind analyses for H*Wind (dashed contours) and the AOC (solid contours) are shown along with the NARR (shaded contours) for Ivan, Rita, and Katrina (Fig. 9). The times selected were driven by the presence of proximity buoy observations that are shown in the accompanying cross sections (Fig. 10). In each of the storms, the NARR fails to capture the detail of the inner-core storm structure. In the Ivan example shown (Fig. 9a), the NARR center is displaced southwest of the best-track position. Despite the offset, the AOC is able to relocate the center and yields an inner-core analysis that is consistent with H*Wind. The impact of the shift in storm position and the broad nature of the NARR wind field can be seen in the W–E cross section, as a local minimum in the wind speed around 50 n mi west of the storm center (Fig. 10a). This AOC feature disappears for the larger blending widths (e.g., EXP3 and EXP5). Given that the analyses are targeted for ensemble wave forecasts with many track, structure, and intensity permutations, the blending width might, in the future, be more strongly coupled to the forecast wind radii. Both the H*Wind and AOC depict the asymmetry, with the strongest winds on the east side of the storm. The H*Wind eyewall is a bit tighter, however. In this case, all three analyses are in agreement with the buoy observation (42001) 124 n mi west of the storm center (the buoy is actually 0.3° north of due west). Buoy 42003, 100 n mi east of the storm, lies midway between the H*Wind analysis and the AOC and is best fit to the storm structure in EXP5. The H*Wind Katrina analysis (taken near peak intensity) has somewhat more asymmetry than does that of the AOC, with a slightly elongated (contracted) wind field along the N–S (W–E) axes (Fig. 9b). Both H*Wind and the AOC wrap a wind maximum (120 kt) around the north side of the storm. However, the AOC brings the wind maximum farther into the NW quadrant to the west of the storm center and it is displaced radially outward from that of H*Wind.

TABLE 4. Moderate TCs (Saffir–Simpson categories 1–2).

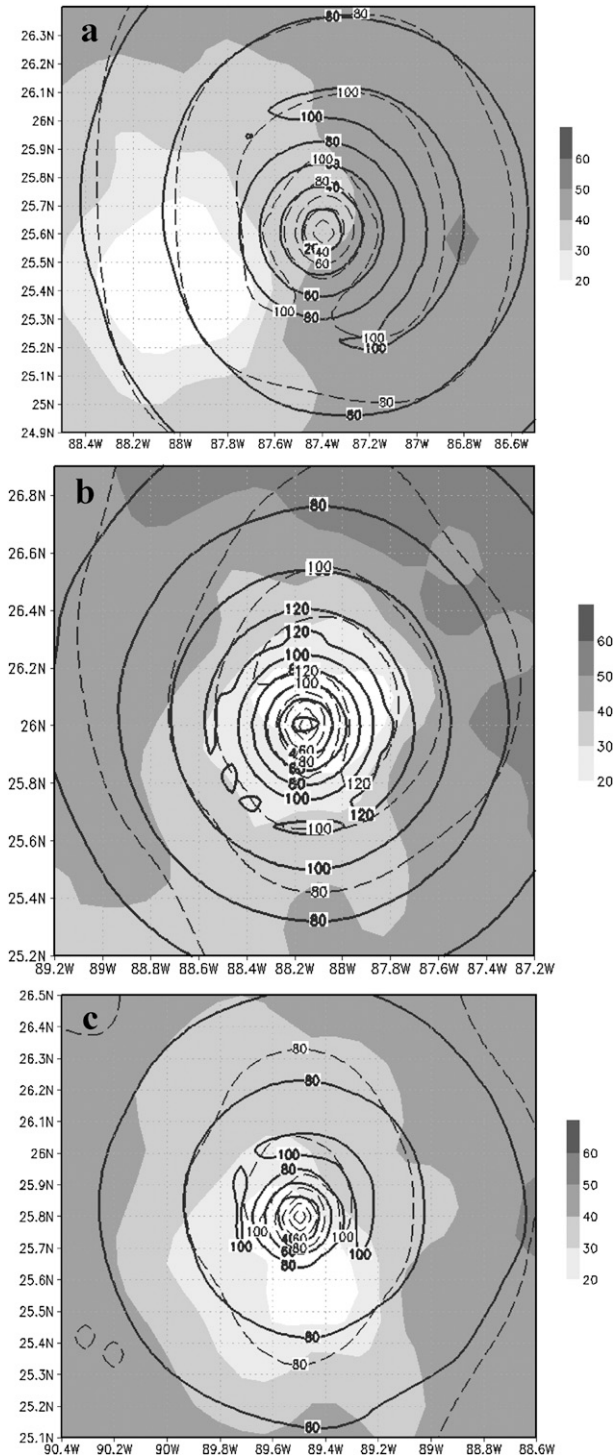| Storm	Saffir–Simpson category	Evaluation period
Earl (1998)	2	1200 UTC 31 Aug–1200 UTC 4 Sep
Georges (1998)	2	1200 UTC 23 Sep–600 UTC 1 Oct
Ike (2008)	2	0000 UTC 9 Sep–0000 UTC 14 Sep
Ida (2009)	2	0600 UTC 6 Nov–0600 UTC 11 Nov

FIG. 9. Horizontal cross sections of the 10-m wind speed (kt) for (a) Ivan valid 0600 UTC 15 Sep 2004, (b) Katrina valid 1500 UTC 28 Aug 2005, and (c) Rita valid 2100 UTC 22 Sep 2005. Shown are the AOC (solid contours), H*Wind (dashed contours), and NARR (shaded). For Rita, H*Wind is valid at 2230 UTC.
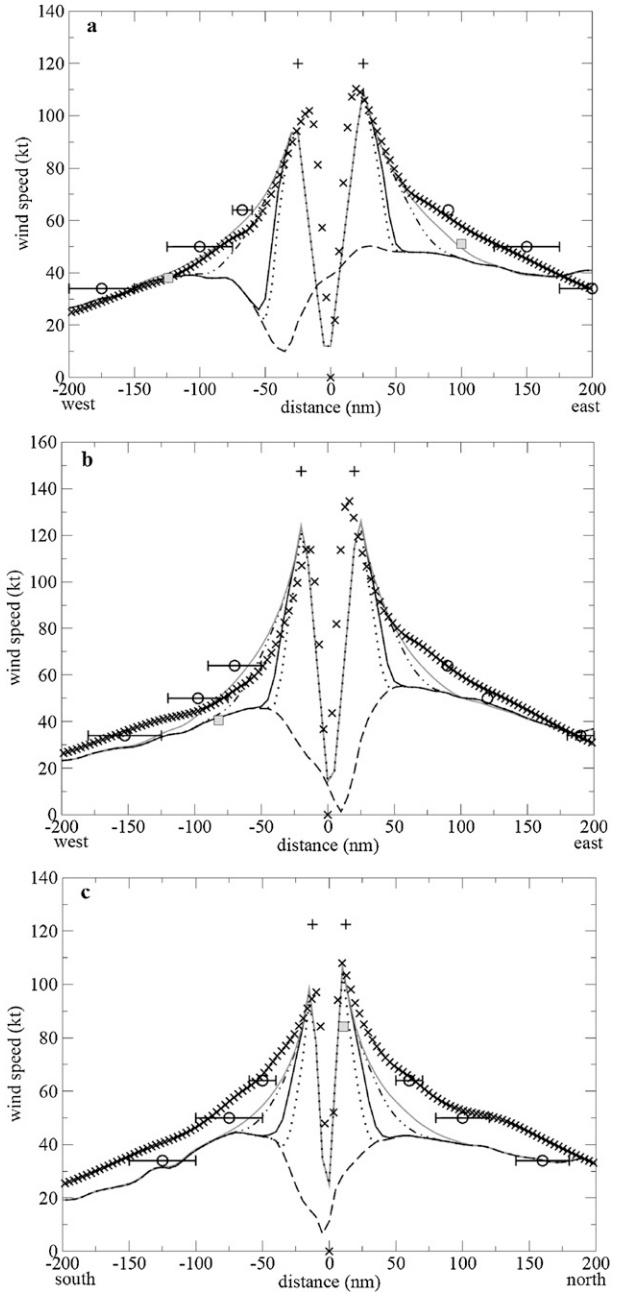

FIG. 10. As in Fig. 8, but for (a) Ivan (west–east) valid 0600 UTC 15 Sep 2004, (b) Katrina (west–east) valid 1500 UTC 28 Aug 2005, and (c) Rita (south–north) valid 2100 UTC 22 Sep 2005.

As in the 1800 UTC W–E cross section (Fig. 8a), the 1500 UTC buoy wind speed 82 n mi west of the storm center is close to that of the AOC (and below that of H*Wind and the best-track wind radii; Fig. 10b). The Rita analyses exhibit somewhat of a different structure from that of the other storms shown, with a relatively tight inner core embedded within a relatively relaxed outer wind field (Fig. 9c). In terms of this structure, the
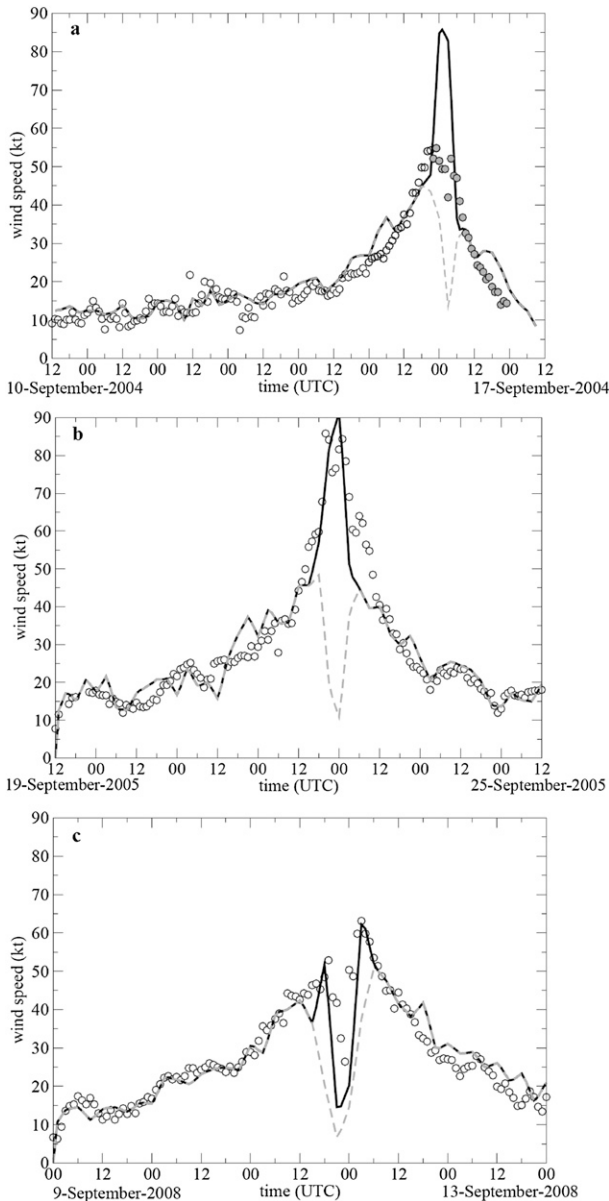
FIG. 11. The U_{10} (kt) time series for NARR (dashed gray line), analysis (solid black line), and buoy (open circles) at buoys (a) 42040 (Ivan), (b) 42001 (Rita), and (c) 42001 (Ike).

TABLE 5. NARR and analysis (BLND) 10-m wind speed (U_{10}) bias (m s^{-1}), RMSD (m s^{-1}), SI, total number of observations for all storms, and missing data.

U_{10}	NARR	BLND	No. of data points	Miss data
Bias	0.04	0.22	8542	144
RMSD	2.8	2.28		
SI	0.30	0.24		

AOC or H*Wind result, both of which indicate a maximum wind speed around 110 kt.

2) TIME SERIES

Time series of U_{10} at NDBC buoy 42001 are shown for Rita and Ike and at 42040 for Ivan in Fig. 11. The U_{10} for the AOC (solid line), buoy (circles), and the NARR (dashed gray line) are shown in each panel in Fig. 11. In each of these three cases the cyclones passed very close to the buoys. For both Rita and Ike, the analysis better resolves the inner-core wind field compared to the NARR. In particular, there is a large discrepancy between the peak wind speed in the analysis versus that of the NARR associated with the passage of TC Rita. In this case, the NARR underforecasts the peak winds by more than 20 m s^{-1}, whereas the analysis peak is close to that observed. During this time, wave heights monotonically increase to near 12 m (see Part II). For TC Ivan, the analysis appears to overestimate the maximum wind speed observed at buoy 42040. Note, however, that the buoy broke loose of its mooring around 2100 UTC 15 September 2004 (filled circles in Fig. 11a), drifting southwest and then southeast over the latter 36 h of the analysis period (Stone et al. 2005). While the buoy reported a maximum wind speed near 27 m s^{-1}, the NHC best track indicates a maximum wind speed of 57 m s^{-1}, a radius of maximum wind of 20 n mi, and a position about 35 km (19 n mi) south of the anchored buoy location at 0000 UTC 16 September 2004. Given that the buoy appears to be situated near the eyewall, any drift may result in significant wind speed discrepancies. While previous data were presented in nautical miles and knots (consistent with best track), the error statistics that follow use the meter–kilogram–second (MKS) convention.

3) BULK

Table 5 lists error statistics, the amount of buoy data used for validation, and the number of missing observations for all storms. The U_{10} bias is quite low and is slightly better for the NARR while the RMSD is about 0.5 m s^{-1} lower for the analysis. The SI is also slightly lower for the AOC. Given that the analysis increases the wind speeds, it is no surprise that the U_{10} analysis

AOC is consistent with H*Wind. Both analyses wrap a 100-kt wind maximum around the north and west sides of the storm—although as with Katrina, the AOC wind maximum is displaced slightly outward from that of H*Wind. Again, there is a slight elongation in the N–S direction in the H*Wind analysis. The wind asymmetry is evident in the S–N cross section (Fig. 10c), with the strongest winds on the north side of both the AOC and H*Wind. The 2100 UTC buoy (42001) wind speed (84 kt) 11 n mi north of the storm is less than either the
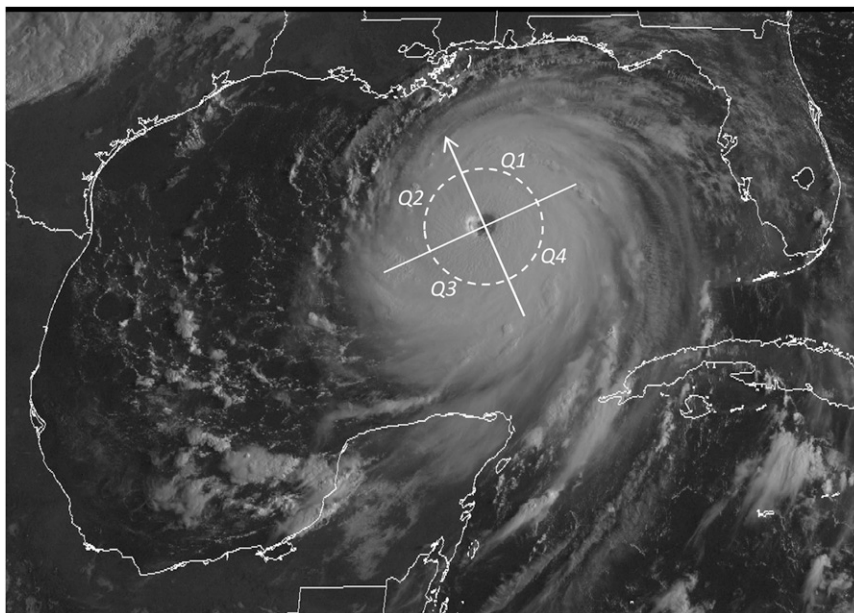
FIG. 12. Visible satellite image of Hurricane Katrina valid 1325 UTC 28 Aug 2005. Storm motion is indicated by the arrow and the four storm-relative quadrants are labeled Q1–Q4. Data obtained from the National Oceanic and Atmospheric Administration (NOAA) Comprehensive Large Array-data Stewardship System (CLASS) server. Dashed circle depicts the 100-n mi radius.

bias is slightly larger than the NARR (both are positive). However, the amount of proximity buoy data (i.e., at small radii) where the blending is important is over-whelmed by the bulk of the observations, which lie on the periphery of the storms where the background wind field is of relatively good quality. Hereafter, with the exception of storm intensity, the bias and RMSD are presented only for observations that lie within 100 n mi of the storm center.

4) STRATIFICATION BY STORM CHARACTERISTICS

The statistics are stratified by storm-relative quadrant (i.e., with respect to TC motion), storm intensity (Saffir–Simpson category), r_m, and storm translation speed. This approach is designed to allow for a more physical as-sessment of the varying wave field in a TC environment (Part II). Moon et al. (2004b) show that the translation speed plays a critical role in determining the wave age and drag coefficient; both of which vary by storm quadrant. Storm intensity is important as well, with re-cent studies indicating a leveling off or reduction in drag at high wind speeds. Four storm-relative quad-rants (Q1–Q4) are defined counterclockwise, starting from the right-front quadrant (Q1) with respect to storm motion, for which the statistics are separately analyzed. An example is shown for Hurricane Katrina (Fig. 12) at 1325 UTC 28 August 2005. Also shown is the storm motion and 100-n mi radius (dashed circle) by which the

error statistics are separated. The radius was selected because it represents the maximum extent of the filter width as r_m and x approach zero (Fig. 6). All statistics hereafter are stratified with respect to these four storm-relative quadrants and the 100-n mi radial distance from the TC center.

Bias, RMSD, and SI for the analysis and NARR winds, the latter of which is also segregated by the 100-n mi radius, are shown for moderate and strong storms (Fig. 13 and Table 7). Clearly, the NARR winds beyond the 100-n mi radius (Fig. 13, gray filled triangles) exhibit small bias and have relatively low RMSD. Within 100 n mi, the NARR wind speeds are low biased, with the largest negative values in Q1 and Q4 (Q2 and Q3) for moderate (strong) storms. The NARR RMSD is similar to the bias, with the largest values in Q1 and Q4 (Q2 and Q3) for the moderate (strong) storms and is largest overall in Q3 for strong storms. The differences between the NARR and analysis SI are much larger for the strong storms. The impact of the analysis is dramatic, with a bias reduction in all quadrants for both moderate and strong storms. The analysis bias is less, however, in each of the four quadrants for the moderate storms. Con-versely, the reduction in the analysis RMSD is greatest for the strong storms. In addition to the error statistics, the amount of buoy data within the respective quadrants and outside (inside) of the 100-n mi radius is given in Table 6 (Tables 7–9). As is the case with all the stratified
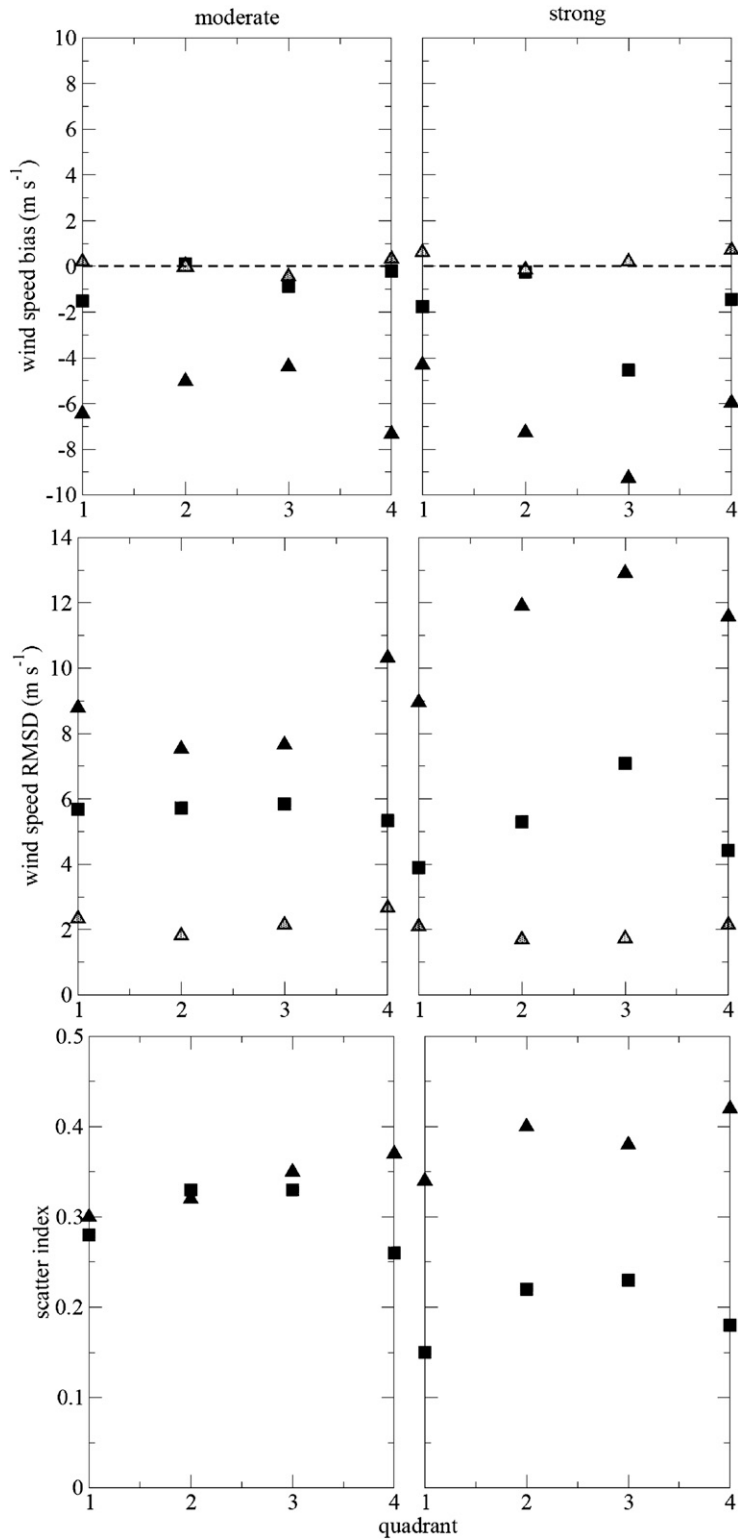
FIG. 13. Storm motion–relative error statistics (by quadrant) for the background (NARR, filled triangles) and analysis (BLND, filled squares) for (left) moderate and (right) strong storms. NARR and analysis statistics (top) wind speed bias (m s^{-1}), (middle) wind speed RMSD (m s^{-1}), and (bottom) SI are shown for data inside (black fill) and outside (gray fill) a 100-n mi radius.

TABLE 6. Number of observations by quadrant (see Fig. 10) for the various stratified statistical subsets and $r > 100$ n mi.

	$r > 100$ n mi			
	Q2	Q3	Q1	Q4
	Left		Right	
Moderate	689	479	771	809
Strong	1284	1172	1503	1507
RMG20	996	1460	1125	1873
RML20	977	191	1149	443
Slow TCs	1448		2424	
Fast TCs	2176		2166	

statistics, the amount of validation (buoy) data is greatly reduced within the 100-n mi radius.

The model and buoy data (within 100 n mi only) for the strong and moderate TCs are combined and stratified with respect to the best-track r_m and presented in Table 8. Note that r_m is selected because it is related to the size of the TC and is used herein to estimate the filter width. Based on examination of the data, an r_m value of 20 n mi is chosen such that the data are relatively evenly split above and below this threshold. Hereafter, values of r_m greater than or equal to (less than) 20 n mi are referred to RMG20 (RML20). As one might expect for the NARR, the RML20 RMSD is larger for all quadrants compared to RMG20 and is largest on the right side (quadrants Q1 and Q4). For RMG20, the NARR wind bias is most negative and the RMSD is largest on the left side (Q2 and Q3) while the opposite is true for RML20, which has the largest negative bias–largest RMSD on the right side. The analysis reduces the RMSD, SI, and bias in all quadrants but has the largest impact for the RML20 storms. Although the overall analysis bias is higher for the RML20 storms, the analysis has a larger impact on the RML20 RMSD, reducing it by over 8.5 m s^{-1} to a value (4.8 m s^{-1}) that is less than its RMG20 counterpart (5.5 m s^{-1}). The overall SI reduction (from 0.46 to 0.19) is larger than for the moderate-to-strong storms. These numbers suggest, in part, that it might be possible to further reduce the errors for the RMG20

storms by enlarging the filter width. However, as is shown in Part II of this paper, the broader and seemingly improved wind field actually increases the wave height error.

The asymmetric structure of the TC wind field is, in part, a function of the storm translation speed. In general, wind speeds increase to the right and decrease to the left of a TC as its speed increases (Schwerdt 1979). In addition, the wave containment time, and ultimately the amount of wave enhancement, is critically linked and extremely sensitive to storm motion and speed (Bowyer and MacAfee 2005). Data from moderate and strong TCs are combined and are stratified with respect to storm translation speed. A storm speed threshold value of 10 kt is chosen here, in part because it represents the lower bound for which the fetch enhancement is maximized (Bowyer and MacAfee 2005) while maintaining a relatively even data distribution. TCs with storm speeds greater than or equal to (less than) 10 kt are referred to as fast (slow) TCs hereafter. Wind speed bias and RMSD for fast and slow TCs are discussed with respect to two storm-relative quadrants here in which Q1 and Q4 (Q2 and Q3) comprise the right (left) quadrant. Statistics are shown for radii within 100 n mi of the TC center only (Table 9).

Overall, the NARR bias and RMSD are largest on the left side of the slow TCs. For the fast TCs only, the NARR bias and RMSD are larger on the right side. The analysis bias reduction is on the order of 5 m s^{-1} for the left and right sides of the slow and fast storms, and is largest on the right side for fast TCs. The analysis RMSD is also around 5 m s^{-1} lower for all but the left side of the fast TCs. The SI is consistent with the RMSD with the analysis showing a decrease on the order of 0.15 with the exception of the left quadrant of fast TCs. In addition, the largest RMSD decrease, on the left side of the slow TCs, is associated with the largest SI drop (0.18) of the left–right quadrants. Although the maximum RMSD for the NARR occurs in the left quadrant for slow storms, the analysis has an RMSD maximum in the left quadrant for fast storms, but the bias is relatively low there. The

TABLE 7. Storm motion–relative error statistics by quadrant (see Fig. 10) for the background (NARR) and analysis (BLND) as a function of storm intensity (strong and moderate, Tables 3 and 4, respectively). Statistics shown are for $r < 100$ n mi only. The all column represents the total for the four quadrants.

U_{10}	Moderate					Strong				
	Q1	Q2	Q3	Q4	All	Q1	Q2	Q3	Q4	All
NARR bias	−6.44	−5.02	−4.38	−7.34	−5.73	−4.31	−7.27	−9.27	−5.97	−6.06
BLND bias	−1.52	0.10	−0.87	0.16	−0.53	−1.76	−0.25	−4.54	−1.44	−1.77
NARR RMSD	8.79	7.53	7.66	10.46	8.61	8.96	11.91	12.91	11.58	10.93
BLND RMSD	5.68	5.72	5.85	5.23	5.64	3.90	5.30	7.09	4.42	4.90
NARR SI	0.30	0.32	0.35	0.37	0.34	0.34	0.40	0.38	0.42	0.39
BLND SI	0.28	0.33	0.33	0.26	0.30	0.15	0.22	0.23	0.18	0.20
No. of data points	41	46	43	38	168	62	32	23	43	160

TABLE 8. Storm motion–relative error statistics by quadrant (see Fig. 10) for the background (NARR) and analysis (BLND) as a function radius of maximum winds r_m for moderate and strong storms combined. RMG20 (RML20) represents storms with $r_m \geq (<)$ 20 n mi. Statistics shown are for $r < 100$ n mi only. The all column represents the total for the four quadrants.

	RMG20					RML20				
U_{10}	Q1	Q2	Q3	Q4	All	Q1	Q2	Q3	Q4	All
NARR bias	−4.16	−6.54	−6.20	−4.75	−5.32	−7.95	−3.95	−5.57	−11.60	−7.69
BLND bias	−1.51	−0.09	−2.38	0.08	−0.98	−2.10	0.12	−1.13	−2.75	−1.63
NARR RMSD	6.67	9.14	9.56	8.49	8.40	13.27	10.89	10.90	16.06	13.31
BLND RMSD	4.50	6.17	6.72	4.39	5.45	5.20	2.54	3.99	5.82	4.75
NARR SI	0.26	0.32	0.36	0.35	0.33	0.42	0.49	0.54	0.40	0.46
BLND SI	0.21	0.31	0.31	0.22	0.27	0.19	0.12	0.22	0.19	0.19
No. of data points	76	60	54	59	249	27	18	12	22	79

analysis RMSD is lower, in the respective quadrants, for slow TCs compared to the fast TCs. Clearly, the NARR impacts the analysis: when the bias in the former is relatively large, it remains so in the latter. However, this does not appear to be the case for the fast TC analysis RMSD, where it is lowest on the right side, which has the largest background RMSD. Wind speed error is critical in terms of wave heights, particularly in extreme events (Cardone et al. 1996), while bias reduction is an essential component in terms of generating skillful ensembles (Hamill 2000). Efforts to further reduce the analysis error (RMSD) by decreasing the blending width reintroduces the low bias inherent in the NARR (within 100 n mi) and, in light of the analysis sensitivity to the bias (section 4b), are not prudent.

5. Discussion and issues

The difference between the fast and slow TCs may, in part, be due to the limitations of the simple parametric model used here. The model depicts wavenumber 1 asymmetries only, and thus complex asymmetries will be problematic (K07). For example, a double-eyewall structure where the wind field exhibits multiple maxima along a radial cannot be recovered by a simple first-order parametric representation of the wind field. If either the observed asymmetry factor or its degree of rotation [see Eq. (1)] differs from the climatological values used here, the estimation of wind radii will be influenced. The climatological asymmetry factor and the degree of rotation depend on storm speed and latitude only. Different parameterizations of these factors and an extension of the parametric model to include higher-order asymmetries would be instructive.

Although the blending between the NARR and AOC is smooth, the analysis wind field tends to decrease more rapidly along a radial than does H*Wind or the best track, especially for TCs with relatively small r_m. This is primarily an artifact of the blending width and can produce a wind speed profile that undershoots the

NARR as the analysis asymptotically approaches the background (e.g., see Fig. 8b). Although this has little or no impact on the forecast wave field (Part II), as demonstrated here, it can be mitigated by increasing the influence of the parametric wind field outward from the storm center. The best approach would be a modification of the simple parameterization used here [Eq. (9)], such that the filter stop end depends on matching the vortex wind speed with that of the background. Currently, the filter stop end is calculated as a residual (i.e., a difference between the filter width and pass end). Alternatively, the bulk estimate of c [Eq. (9)] as defined for the AOC (50 n mi) was selected based on all (12) of the storms. Allowing c (and thus D) to vary as a function of the distance between r_m and either the 64- or 50-kt radii is worth investigating. In some cases, the NARR eye is offset from the "official" location in the best-track data. A higher-resolution and improved background field will likely alleviate some, but not all, of these mismatches. The intent of this study is to lay the groundwork for using short-term (i.e., on the order of a day) forecast track–intensity permutations and associated parameters generated by the operational (NHC) Monte Carlo model

TABLE 9. Storm motion–relative error statistics (m s^{-1}, by quadrant) for the background (NARR) and analysis (BLND) as a function of storm speed for moderate and strong storms combined. Statistics shown are for $r < 100$ n mi only. Slow (fast) TCs have storm motions $< (\geq)$ 10 kt. Left (right) includes storm quadrants Q2 and Q3 (Q1 and Q4) as shown in Fig. 12.

	Slow TCs		Fast TCs	
	Q2/Q3	Q1/Q4	Q2/Q3	Q1/Q4
U_{10}	left	right	left	right
NARR bias	−7.14	−5.29	−5.39	−6.39
BLND bias	−2.04	−0.35	−0.44	−2.27
NARR RMSD	10.95	9.30	8.92	10.58
BLND RMSD	5.11	4.48	6.31	5.04
NARR SI	0.41	0.36	0.36	0.37
BLND SI	0.23	0.21	0.32	0.20
No. of data points	51	99	93	85

(DeMaria et al. 2009) to generate wave ensembles. Under this paradigm, even short-term track forecasts can have considerable spread. In this case it will, in general, be better to remove the background vortex altogether, hole fill the wind field, and then generate an analysis for a given forecast time (e.g., Sampson et al. 2010). This approach is economical in the sense that it uses a single background field, for a given forecast time, that can then be merged with the Monte Carlo realizations. Nonetheless, this still requires $N \times F/n$ distinct analyses and wave model simulations, where N is the number of realizations, F the forecast cycle length (in h), and n the wind forcing interval (in h). Hence, unlike the long-term wave hindcast studies previously discussed, the computational challenge here is not the resolution of the atmospheric model, but rather the number of wind analyses and subsequent wave forecasts. In terms of the latter, the cubic relationship between the resolution and computational time is obviously problematic from an operational perspective.

Despite adjusting the buoy wind speeds to 10 m, it is possible that the speeds remain low biased as a result of temporal averaging and high gustiness (Cardone et al. 1996). However, if this is the case, then the first-guess low bias that is prevalent in all quadrants within the 100-n mi radius is actually worse than shown here. In addition, no static stability corrections were applied. However, these are not likely large for a GOM TC environment (Powell et al. 2003). The sparseness of the buoy observations is likely more important here, making it difficult to effectively tune the analysis parameters. In terms of the analysis, the low wind bias can be mitigated by increasing the grid resolution from the 10 km used herein. However, experiments for which the wind analysis resolution was reduced to 6 km (not shown) did not result in improved wave forecasts (Part II). In addition, whatever benefits increased spatial resolution provides must be considered in the context of maintaining computational efficiency, that latter of which is a key element driving the configuration presented here.

REFERENCES

Barnes, S. L., 1964: A technique for maximizing details in numerical weather map analysis. *J. Appl. Meteor.,* **3,** 396–409.

Benjamin, S. G., and N. L. Seaman, 1985: A simple scheme for objective analysis in curved flow. *Mon. Wea. Rev.,* **113,** 1184–1198.

Berg, R., 2009: Hurricane Ike (AL092008) 1–14 September 2008. National Hurricane Center Tropical Cyclone Rep., 55 pp.

Bowyer, P. J., and A. W. MacAfee, 2005: The theory of trapped-fetch waves with tropical cyclones—An operational perspective. *Wea. Forecasting,* **20,** 229–244.

Butterworth, S., 1930: On the theory of filter amplifiers. *Wireless Eng.,* **7,** 536–541.

Cardone, V. J., R. E. Jensen, D. T. Resio, V. R. Swail, and A. T. Cox, 1996: Evaluation of contemporary ocean wave models in rare extreme events: The ''Halloween Storm'' of October 1991 and the ''Storm of the Century'' of March 1993. *J. Atmos. Oceanic Technol.,* **13,** 198–230.

——, A. T. Cox, and V. R. Swail, 1999: Evaluation of NCEP reanalysis surface marine wind fields for ocean wave hindcasts. Preprints, *CLIMAR 1999,* Vancouver, BC, Canada, Joint WMO/IOC Technical Commission for Oceanography and Marine Meteorology (JCOMM), 68–85.

——, ——, and ——, 2000: Specification of global wave climate: Is this the final answer? *Proc. Sixth Int. Workshop on Wave Hindcasting and Forecasting,* Monterey, CA, Environment Canada–U.S. Army Engineer Research and Development Center's Coastal and Hydraulics Laboratory–JCOMM, 211–223.

——, ——, and G. Z. Forristall, 2007: Hindcast of winds, waves and currents in northern Gulf of Mexico in Hurricanes Katrina (2005) and Rita (2005). *Proc. Offshore Technology Conference,* Houston, TX, OTC 18652.

Chen, H. S., 2006: Ensemble prediction of ocean waves at NCEP. *Proc. 28th Ocean Engineering Conference,* Kaohsiung, Taiwan, National Sun Yat-Sen University, 10 pp.

Cressman, G. P., 1959: An operational objective analysis system. *Mon. Wea. Rev.,* **87,** 367–374.

DeMaria, M., S. D. Aberson, K. V. Ooyama, and S. J. Lord, 1992: A nested spectral model for hurricane track forecasting. *Mon. Wea. Rev.,* **120,** 1628–1643.

——, J. A. Knaff, R. Knabb, C. Lauer, C. R. Sampson, and R. T. DeMaria, 2009: A new method for estimating tropical cyclone wind speed probabilities. *Wea. Forecasting,* **24,** 1573–1591.

Demuth, J., M. DeMaria, and J. A. Knaff, 2006: Improvement of Advanced Microwave Sounder Unit tropical cyclone intensity and size estimation algorithms. *J. Appl. Meteor. Climatol.,* **45,** 1573–1581.

Desjardins, S., R. Lalbeharry, H. Ritchie, and A. Macafee, 2004: Blending parametric hurricane surface fields into CMC forecasts and evaluating impact on the wave model of hurricane Juan and others. *Proc. Eighth Int. Workshop on Wave Hindcasting and Forecasting,* Oahu, HI, Environment Canada–U.S. Army Engineer Research and Development Center's Coastal and Hydraulics Laboratory–JCOMM, F2.

Gilhousen, D. B., 1987: A field evaluation of NDBC moored buoy winds. *J. Atmos. Oceanic Technol.,* **4,** 94–104.

——, 2006: A complete explanation of why moored buoy winds are less than ship winds. *Mar. Wea. Log,* **50,** 4–7.

Hamill, T. M., 2000: Interpretation of rank histograms for verifying ensemble forecasts. *Mon. Wea. Rev.,* **129,** 550–560.

——, S. L. Mullen, C. Snyder, D. P. Baumhefner, and Z. Toth, 2000: Ensemble forecasting in the short to medium range: Report from a workshop. *Bull. Amer. Meteor. Soc.,* **81,** 2653–2664.

Holt, M. W., and B. J. Hall, 1992: A comparison of 2nd generation and 3rd generation wave model physics. Met Office Short-Range Forecasting Research Division Tech. Rep. 10, 23 pp.

Hsu, S. A., E. A. Meindl, and D. B. Gilhousen, 1994: Determining the power-law wind-profile exponent under near-neutral stability conditions at sea. *J. Appl. Meteor., 33,* 757–765.

Janssen, P. A. E. M., B. Hansen, and J. R. Bidlot, 1997: Verification of the ECMWF wave forecasting system against buoy and altimeter data. *Wea. Forecasting, 12,* 763–784.

Kalnay, E., and Coauthors, 1996: The NCEP/NCAR 40-Year Reanalysis Project. *Bull. Amer. Meteor. Soc., 77,* 437–471.

Knaff, J. A., C. R. Sampson, M. DeMaria, T. P. Marchok, J. M. Gross, and C. J. McAdie, 2007: Statistical tropical cyclone wind radii prediction using climatology and persistence. *Wea. Forecasting, 22,* 781–791.

Lazarus, S. M., S. T. Wilson, M. E. Splitt, and G. A. Zarillo, 2013: Evaluation of a wind–wave system for ensemble tropical cyclone wave forecasting. Part II: Waves. *Wea. Forecasting, 28,* 316–330.

Makin, V. K., and V. N. Kudryavtsev, 1999: Coupled sea surface-atmosphere model 1. Wind over waves coupling. *J. Geophys. Res., 104* (C4), 7613–7623.

Mishra, S. K., 2007: NLINLS: A differential evolution based nonlinear least squares Fortran 77 program. Social Science Research Network, 10 pp. [Available online at http://mpra.ub.uni-muenchen.de/4949/1/MPRA_paper_4949.pdf.]

Moon, I. J., I. Ginis, and T. Hara, 2004b: Effect of surface waves on air–sea momentum exchange. Part II: Behavior of drag coefficient under tropical cyclones. *J. Atmos. Sci., 61,* 2334–2348.

Mousavi, S. M., F. Jose, and G. Stone, 2009: Simulating Hurricane Gustav and Ike wave fields along the Louisiana Innershelf: Implementation of an unstructured third-generation wave model, SWAN. *Oceans 2009—Marine Technology for Our Future: Global and Local Challenges,* Biloxi, MS, MTS/IEEE.

Powell, M. D., S. H. Houston, L. R. Amat, and N. Morisseau-Leroy, 1998: The HRD real-time hurricane wind analysis system. *J. Wind Eng. Indust. Aerodyn., 77–78,* 53–64.

——, P. J. Vickery, and T. A. Reinhold, 2003: Reduced drag coefficient for high wind speeds in tropical cyclones. *Nature, 422,* 279–283.

Roulston, M. S., J. Ellepola, J. Hardenberg, and L. A. Smith, 2005: Forecasting wave height probabilities with numerical weather prediction models. *J. Ocean Eng., 32,* 1841–1863.

Sampson, C. R., P. A. Wittman, and H. L. Tolman, 2010: Consistent tropical cyclone wind and wave forecasts for the U.S. Navy. *Wea. Forecasting, 25,* 1293–1306.

Schwerdt, R. W., F. P. Ho, and R. R. Watkins, 1979: Meteorological criteria for standard project hurricane and probable maximum hurricane wind fields, Gulf and east coasts of the United States. NOAA Tech. Rep. NWS 23, 317 pp.

Stone, G. W., N. D. Walker, S. A. Hsu, A. Babin, B. Liu, B. D. Keim, W. Teague, D. Mitchell, and R. Leben, 2005: Hurricane Ivan's impact along the northern Gulf of Mexico. *Eos, Trans. Amer. Geophys. Union, 86,* 497–500.

Storn, R., and K. Price, 1997: Differential evolution—A simple and efficient heuristic for global optimization over continuous spaces. *J. Global Optim., 11,* 341–359.

Uhlhorn, E. W., P. G. Black, J. L. Franklin, M. Goodberlet, J. Carswell, and A. S. Goldstein, 2007: Hurricane surface wind measurements from an operational stepped frequency microwave radiometer. *Mon. Wea. Rev., 135,* 3070–3085.

Young, I. R., 2003: A review of the sea state generated by hurricanes. *Mar. Struct., 16,* 210–218.